JOURNAL OF GUIDANCE, CONTROL, AND DYNAMICS
Vol. 33, No. 1, January–February 2010

Integration of Hydraulic Lag-Damper Models with Helicopter Rotor Simulations

Branislav Titurus* and Nick Lieven†
University of Bristol, Bristol, England BS8 1TR, United Kingdom

DOI: 10.2514/1.41961

This paper describes the design and integration of a generic hydraulic lag-damper model into an industrial helicopter rotor simulation code. The paper explains the details of an implementation of a computational platform integrating the rotor simulation code with a damper model. A parametric physical damper model is developed here in order to allow physically consistent improvements to helicopter performance studies. Further, this model enables investigating novel uses of lag dampers, such as for vibration reduction. The physical consistency of this work is demonstrated in two case studies. In the first instance, the damper laboratory experimental data are used for a correlation and validation study illustrating the capability of the modeling methodology to generate the model with refined response predictions. The second case study considers a physics-based lag-damper model with an active flow restrictor based on a modified version of the validated passive damper model. This realistic model is shown to be able to induce physically consistent changes in the nonrotating rotor-hub responses. A parametric study with harmonic three-per-revolution flow-restrictor activity suggests that significant load changes are possible in the nonrotating in-plane hub forces and moment. The study also shows possible tradeoffs such as high damper peak forces corresponding to the reduced in-plane forces. Therefore, the presence of these tradeoffs will require the use of constrained optimization formulation to address more complex problem configurations.

Nomenclature

A_A	=	effective cross section of the flow restrictor
A_P	=	cross-sectional area of the symmetric piston
A_V	=	cross-sectional area of the valve-seat aperture
$\mathcal{B}$	=	multiplicator specifying event-based flow conditions
B_0	=	constant bulk modulus of hydraulic fluid
C_D	=	discharge coefficient
$\mathcal{D}_{\text{feas}}$	=	subset of the activity parameter space
d_V	=	diameter of the cross-sectional area of the valve-seat aperture
$\mathbf{e}_{DC}$	=	unit vector in the direction of the damper centerline
F_D	=	damper force
F_X, F_Y, F_Z	=	nonrotating hub forces
F_f	=	friction force
F_{hydro}	=	model of the relief-valve excitation force
$F_{\circ,\cos}$, $F_{\circ,\sin}$	=	harmonic (Fourier) cosine and sine components of the fixed hub force
$\mathbf{f}(\circ)$, $\mathbf{f}_i(\circ)$	=	damper state-space model
$f_{D,i}$	=	lag-damper ith modal load
$f_{i,j}$	=	ith modal load caused by the jth physical effect
f_{rot}	=	fundamental rotational frequency
I_i, ς_i, $\omega_{0,i}$	=	ith modal mass, damping ratio, and undamped natural frequency of the blade
ML_i	=	modal loads of the ith blade mode shape
M_X, M_Y, M_Z	=	nonrotating hub moments
$M_{\circ,\cos}$, $M_{\circ,\sin}$	=	harmonic (Fourier) cosine and sine components of the fixed hub moment
m_P	=	mass of the piston
m_V, b_V, k_V	=	effective mass, damping, and stiffness of the valve oscillator
N_D	=	number of the local degrees of freedom of the blade
N_{damper}	=	number of the damper internal steps per one rotor step
N_m	=	number of the modes used in the modal representation
N_P	=	total number of the physical parameters
N_{rotor}, N_ψ	=	total number of rotor steps per one revolution
N_π	=	number of flow-restricting elements
$\mathbf{P}_{EC}$	=	static force transfer matrix
$\mathbf{p}$	=	vector of physical or activity parameters
p	=	absolute and homogeneous pressure in the fluid container
Q	=	volumetric flow rate
$\mathbf{q}$	=	vector of the modal displacements
$q(\circ)$	=	flow-pressure static characteristics
q_i	=	ith modal displacement
q^{-1}	=	inverse of the function q
$\text{sign}(\circ)$	=	signum function.
$\mathbf{T}$	=	orthogonal matrix representing rotational transformation
$\mathbf{t}_{DC}$	=	transformation matrix associated with the local blade coordinate system
$\mathbf{u}$	=	local deformation of the blade point
$\mathbf{u}_0$	=	steady blade deformation due to specified flight conditions
$u(t)$	=	control input signal
V	=	volume of the fluid chamber
X, x	=	normalized and absolute position along the blade length
X_C	=	equivalent valve displacement corresponding the critical pressure differential
X_E	=	normalized position of the damper attachment arm
$\mathbf{x}$	=	state vector of the damper model
xR	=	number of the cycles per one revolution
$x\Omega$	=	angular frequency represented as an integer multiple of the rotating frequency
$\mathbf{x}_{AB}$, $\mathbf{x}_{AC}$, $\mathbf{x}_{BC}$	=	damper piston and blade joint position vectors

Received 2 November 2008; revision received 5 October 2009; accepted for publication 5 October 2009.

*Research Associate, Department of Aerospace Engineering, Queens Building, University Walk.

†Professor, Department of Aerospace Engineering, Queens Building, University Walk.

$\mathbf{x}_{V,i}$ = state vector of the ith relief valve
y_P = piston displacement
α = half-angle of the conically shaped valve's poppet
β = vertical flapping of the blade in the blade attachment joint
β_0 = isothermal tangent compressibility of hydraulic fluid
γ = estimated coefficient of the asymptotic model of the discharge coefficient
ΔP_C = critical valve-activation pressure differential
Δp = pressure difference due to pressure losses
$\Delta\psi$, $\Delta\psi_{\text{dmp}}$ = major rotor azimuth step and minor damper azimuth substep
Δ_q = modal displacement convergence threshold
δ, γ = damper centerline orientation angles with respect to the hub
$\delta(\circ)$ = Dirac delta function
ζ = ratio of the initial volumes of the damper working chambers
η = lead-lag rotation of the blade in the blade attachment joint
θ = control pitch angle
ρ = density of hydraulic fluid
$\mathbf{\Phi}$ = mode-shape matrix
$\boldsymbol{\varphi}_i$ = ith flap-lag-torsion coupled normal mode shape of the blade
ψ = azimuth angle
Ω = fundamental angular frequency

I. Introduction

THIS paper presents work related to the integration of a modular and multifunctional model of a hydraulic lag damper into an aeroelastic helicopter rotor simulation code. A lag damper is a passive energy-dissipating component for which the primary role is to provide damping augmentation for the lead-lag blade motion in unsteady operational regimes. The importance of the lag-damper modeling in the full rotor context stems from the fact that, in certain design configurations, it represents a significant force contributor to the blade loading system. It is therefore desirable to produce and apply a reliable, physically based, parametric model of the damper. This type of damper often uses hydromechanical principles to achieve the required operational characteristics. At the simulation level, assuming a physically based modeling approach, the modeling effort produces a coupled hydromechanical model of the damper. Further, the integration effort produces a multiphysical platform coupling the original rotor-blade aeroelastic model with the hydromechanical model of the lag dampers. The two problems associated with this effort are model coupling and damper modeling. This paper provides a description of the work carried out in both areas.

An early reference that adopts hydraulic system theory in hydraulic actuator modeling was presented by Mitchell and Johnson [1], and a more recent example of this approach in the control design for a hydraulic actuator is given by Yao et al. [2]. Both publications apply standard methodologies and modeling approaches used in hydraulic engineering (e.g., [3]). With increasing computational capability, these more refined techniques have been widely investigated and integrated in mechanical engineering [4–7]. The applications of discrete damping devices in the civil engineering sector are often focused on bridges and high-rise buildings [8,9]. In the aerospace sector, this approach was considered for the case of a passive landing gear (Walls [10] and Wahi [11]) and, more recently, for the case of a semi-active landing gear (Batterbee et al. [12]). A similar modeling approach has been applied to the case of a passive hydraulic lag damper by Eyres et al. [13,14]. The application of this hydromechanical damper model in the helicopter rotor performance studies was summarized in [15], with focus on vibration reduction. One of the general goals in this area is model validation and model refinement. A further research program conducted by the same research groups also focused on the development of a versatile experimental platform. The resulting experimental data allowed the further incremental damper model refinement (Titurus and Lieven [16]). During the same period, a modeling approach based on hydraulic system concepts and applied in a similar setting was presented by Bauchau and Liu [17]. Novel lag-damper concepts that have been investigated recently include elastomeric, magneto-rheological, and magnetorheological fluid-elastic dampers [18–20].

The modeling approaches described above were also applied to investigate the concept of semi-active dampers (e.g., Symans and Constantinou [21], Patten et al. [22], and Heo et al. [23]). The consideration of active components in the rotorcraft sector is not new and the general concept of higher harmonic control has been investigated for at least the past two decades [24,25]. This specific methodology has been recently considered in the context of the semi-active damper located in rotor assemblies acting in both the lead-lag plane and flapping direction in the work by Anusonti-Inthra et al. [26]. This work used a simplified linear dashpot element with variable-damping coefficient adopted from [21]. An analytical investigation of the damper with a single variable flow restrictor is presented by Titurus and Lieven [27]. This study investigates the physical mechanism behind the coupling effects induced by the periodic parameter modulations of the damper with periodic piston excitation. The use of alternative semi-active magnetorheological and fluid-elastomeric lag dampers is considered in [28,29], respectively.

A second element considered in this paper is the coupling of the damper model with established industrial aeroelastic simulation code. A general investigation of the coupling schemes with proposed advanced implicit schemes in an aerospace context was provided by Farhat and Lesoinne [30]. The simulations covering multiple physical domains in a multibody dynamics analysis are addressed by Vaculín et al. [31] and Arnold [32]. The theoretical investigation of the hydromechanical system in hydraulic engineering is presented in [33]. The development of the complex rotor performance prediction code in the industrial setting is illustrated in [34,35].

The modeling approach presented here is a standard approach for hydraulic devices in general and dampers specifically. Current work documents the original development of the damper models and their extensions using the concepts of hydraulic system theory. Demonstrated research is based on the combination of theoretical derivations and experimental observations. The first case study documents this effort. While it is relatively straightforward to apply mentioned theoretical concepts to create models of these devices, it is much more difficult to assure their validity in the broad range of operating conditions. The refinement case-study documents important cases in which consistently underestimated responses provided by the baseline model were improved by confronting this model with experimentally obtained damper data.

A single hydraulic state (pressure differential) is employed in the current damper model [15,27]. The corresponding state equation is derived in [27]. Most other researchers use two-state damper models. There are some advantages associated with single-hydraulic-state damper models. One obvious advantage is the reduced computational effort. However, the primary advantage, from the authors' points of view, is that this form of the model is more amenable to the theoretical analysis [27]. In this model, one state of the damper is directly related to its functionally important response: the damper force.

The research presented here represents a continuation of the previous studies conducted in [13–15]. Recent work that forms a basis for the present work is summarized in [16,27]. In [16] the baseline damper model is compared with experimental data on the basis of which model refinement was suggested. The work presented in [27] provides a consistent analytical framework and a model for dealing with a semi-active hydraulic damper with periodic piston excitation. Other works that can be related to this research are [21,22] for semi-active damper modeling, [26] for the application of semi-active technology in the context of helicopter rotors, and [17], which represents a similar research effort performed in parallel with our research. The application of hydraulic components in the context of flexible multibody systems was already studied in [36]. This work

dealt with the development of the modeling concepts that later became part of the commercial software for simulation of multibody systems [37]. The work presented here concerns the damper model development and its coupling with the industrial aeroelastic helicopter rotor simulation code R150 [34]. Current work demonstrates that through the concept of coupling, the scope of such software tool can be significantly increased and updated. This paper also presents a novel implementation and the related case study investigating the influence of the semi-active lag damper on the nonrotating hub forces. This work extends the work in [26] by considering a realistic physically based model of the semi-active damper. This concept model is based on the validated model of the existing passive hydromechanical damper and it is later applied in a medium-sized production helicopter. In this respect, the goal of this paper is to demonstrate and investigate the effects associated with the semi-active damper with periodic perturbations of its internal parameter by using coupled rotor–damper aeroelastic code and to show its implementation and physical consistency through the analysis provided in the case-study sections.

The paper consists of the following parts: Section I presents an overview of the publications related to the topics developed in this paper. Section II provides a basic outline of the reference industrial computational code with a focus on the elements relevant to the damper model. Section III introduces the theoretical elements and the model of the generic lead-lag damper including its three different specializations. Section IV describes the coupled computational platform integrating the original rotor performance code with the lag-damper code, and the paper concludes with two case studies presented in Sec. V.

II. Lag Damper in Broader Rotor-Helicopter Context

The structural configuration of the lag damper is illustrated in Fig. 1. This section of the paper presents the industrial rotor performance simulation code R150. This code simulates steady flight or maneuver conditions of the helicopter main rotor. The simulation code was produced by the Royal Aircraft Establishment and industry in early 1980s. Its physical and implementation principles are provided by Young [34]. This section presents a description of its features relevant to damper modeling and its coupling with the code.

Figure 1 shows the building blocks of the main rotor based on the symmetric arrangement of a single blade. The hub is represented by the segment *A-B* and rotates with a fixed rotational velocity Ω. The flexible blade is assumed to be attached at the hinge *B*, freeing all three rotational degrees of freedom, where η is the lead-lag rotation in the plane of the rotor, β is the vertical flapping with respect to the plane of the rotor, and θ is the control pitch angle. The lag damper is represented by the segment *D-C* and is attached to the locations on the hub *D* and the blade *C* via ball bearings, ensuring only axial force transfer.

The quantities of interest are the nonrotating hub forces F_X, F_Y, and F_Z and the moments M_X, M_Y, and M_Z, shown in Fig. 1a. The azimuth angle $\psi = \Omega t$ represents the spatial angular position of the investigated quantities. An alternative representation of these quantities, assuming periodic responses during steady flight, will be considered via a normalized frequency-domain representation. The discrete frequency components will be expressed for integer multiples of the fundamental rotational frequency $f_{\text{rot}} = \Omega/2\pi$ in the form κR ($\kappa = 1, 2, \ldots$) for the frequency of κ events per one full rotor cycle.

The damper in its current arrangement is a velocity-sensitive device producing a force along the line of its action *D-C* only when the piston is forced to move by the blade via the attachment point *C*. Figure 1b shows the force due to the projected velocity component $\dot{y}_P \mathbf{e}_{DC}$ of the total velocity $\dot{\mathbf{x}}_{AC}$ at the point *C*. The damper activity can be represented by the two equal and opposite hub and blade forces acting along the line *D-C*. The damper influences the rotor behavior indirectly, where the changes are introduced by affecting the blade vibration patterns. The following relationships are used to include the nonlinear kinematics due to the joint *B*, as shown in Fig. 1:

$$\begin{aligned} \mathbf{x}_{AC}|_{\text{hub}} &= \mathbf{x}_{AB}|_{\text{hub}} + \mathbf{T}(\eta,\beta,\theta)\mathbf{x}_{BC}|_{\text{blade}} \\ [\dot{x}_P, \dot{y}_P, \dot{z}_P]^T|_{\text{damper}} &= \mathbf{T}_{DC}^{-1}(\delta,\gamma)\dot{\mathbf{x}}_{AC}|_{\text{hub}} = \mathbf{T}_{DC}^{-1}(\delta,\gamma)\dot{\mathbf{T}}(\eta,\beta,\theta)\mathbf{x}_{BC}|_{\text{blade}} \end{aligned} \tag{1}$$

where $\mathbf{x}_{AC}$, $\mathbf{x}_{AB}$, and $\mathbf{x}_{BC}$ are the position vectors specified in their respective local coordinate systems according to Fig. 1; labels *hub*, *damper*, and *blade* indicate the quantities specified in the local coordinate systems of the hub, damper, and blade, respectively; η, β, and θ are the lead-lag, flap, and pitch rotation angles applied at the hinge *B*, respectively; the matrix $\mathbf{T}(\eta,\beta,\theta) \in \mathbb{R}^{3\times3}$ ($\mathbf{T}^T\mathbf{T} = \mathbf{I}$) represents the rotational transformation between the *hub* and *blade* in local coordinate systems due to the rotation of the blade around the hinge *B*; $\dot{x}_P$, $\dot{y}_P$, and $\dot{z}_P$ are the components of $\dot{\mathbf{x}}_{AC}|_{\text{hub}}$ expressed in the local coordinate system of the damper via the orientation transformation matrix $\mathbf{T}_{DC}(\delta,\gamma) \in \mathbb{R}^{3\times3}$ ($\mathbf{T}_{DC}^T\mathbf{T}_{DC} = \mathbf{I}$), dependent on the two orientation angles δ and γ, which specifies the position of the *damper* centerline *D-C* with respect to the *hub*.

The local velocity component $\dot{y}_P = \mathrm{d}y_P/\mathrm{d}t$ of the piston attachment point *C* represents effective excitation of the damper. Representation of the matrix $\mathbf{T}(\eta,\beta,\theta)$ as the sequence of the rotations provides the time derivative

$$\begin{aligned} \mathbf{T}(\eta,\beta,\theta) &= \mathbf{T}_\eta(\eta)\mathbf{T}_\beta(\beta)\mathbf{T}_\theta(\theta) \\ \dot{\mathbf{T}}(\eta,\beta,\theta) &= \dot{\mathbf{T}}_\eta\mathbf{T}_\beta\mathbf{T}_\theta + \mathbf{T}_\eta\dot{\mathbf{T}}_\beta\mathbf{T}_\theta + \mathbf{T}_\eta\mathbf{T}_\beta\dot{\mathbf{T}}_\theta \end{aligned} \tag{2}$$

where $\mathbf{T}_\mathcal{I} \in \mathbb{R}^{3\times3}$, $\mathbf{T}_\mathcal{I}^T\mathbf{T}_\mathcal{I} = \mathbf{I}$, and $\mathcal{I} \in \{\eta,\beta,\theta\}$ are the rotational matrices representing rotations in the hinge *B*.

The blade equations are derived with the help of Hamilton's method and the ordering scheme [34,38,39]. Blade equations of motions, including the steady blade loads, are used to establish its modal representation, which then serves to represent the blade motion via the modal summation approach. To include the effect of the point loads, the combination of force integration and modal

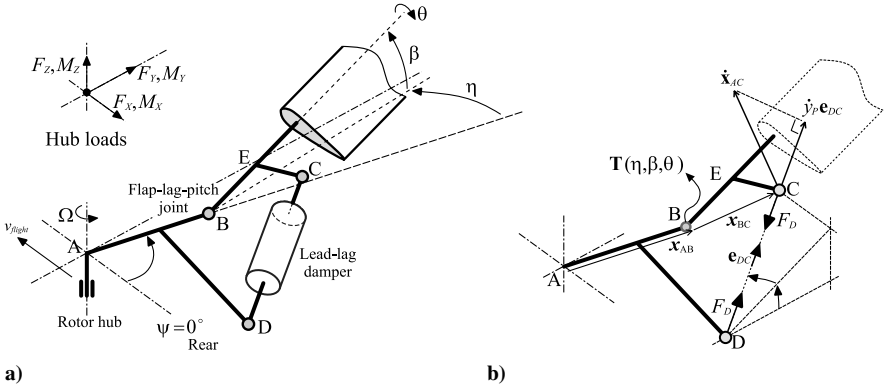

Fig. 1 Schematics of the lag damper within the main rotor substructure: a) general configuration with the lag damper and b) damper loading effect and the principal kinematics.

summation methods is used [35,40]. The physical motion of the blade is represented as follows:

$$\mathbf{u}(X,\psi) = \mathbf{u}_0(X) + \sum_{i=1}^{N_m} q_i(\psi)\boldsymbol{\varphi}_i(X) = \mathbf{u}_0(X) + \boldsymbol{\Phi}(X)\mathbf{q}(\psi)$$
$$\psi \in [0, 2\pi]$$
$$X = \frac{x}{R} \in [X_0, 1] \tag{3}$$

where X is the normalized position along the blade, $X_0 = x_0/R$ is the normalized distance and x_0 is the absolute distance of the blade cutoff for the rotor at a radius R, $\mathbf{u}(X,\psi) \in \mathbb{R}^{N_D}$ is the local deformation of the blade point at the position X and the azimuth angle ψ, $N_D = 6$ is the number of the local degrees of freedom, $\mathbf{u}_0(X) \in \mathbb{R}^{N_D}$ is the steady blade deformation due to inclusion of the external load distribution corresponding to the given flight conditions, q_i are the modal displacements arranged in the vector $\mathbf{q} \in \mathbb{R}^{N_m}$, $\boldsymbol{\varphi}_i(X) \in \mathbb{R}^{N_D}$ is the ith flap-lag-torsion coupled normal mode shape of the blade corresponding to the given flight condition,

$$\boldsymbol{\Phi}(X) = [\boldsymbol{\varphi}_i(X)] \in \mathbb{R}^{N_D \times N_m}$$

is the mode-shape matrix, and N_m is the number of the modes used in the modal representation.

The modal basis $\boldsymbol{\varphi}_i$ $(i = 1, \ldots, N_m)$ is used to produce a set of N_m modal equations of motion for the unknown modal displacements q_i. The nonlinear effects, inertial and external forcing due to aerodynamic effects, are placed on the right-hand side of the following equation:

$$\ddot{q}_i + 2\varsigma_i\omega_{0,i}\dot{q}_i + \omega_{0,i}^2 q_i = \frac{1}{I_i\Omega}\left(\sum_{(j)} f_{i,j}(\mathbf{q},\dot{\mathbf{q}}) + f_{D,i}(\mathbf{q},\dot{\mathbf{q}})\right) \tag{4}$$

where q_i, $\dot{q}_i$, and $\ddot{q}_i$ are the ith modal displacements, velocities, and accelerations further assembled into the vectors of the modal displacements and velocities $\mathbf{q}$ and $\dot{\mathbf{q}} \in \mathbb{R}^{N_m}$, respectively; I_i, ς_i, and $\omega_{0,i}$ are the ith modal mass, damping ratio, and undamped natural frequency, respectively; and $f_{i,j}$ is the ith modal load caused by the jth effect, including inertial, aerodynamic, and structural influences. The loads due to the lag damper $f_{D,i}$ are separated from the other loads.

The set of equation (4) is solved for the modal responses $\mathbf{q}(\psi)$ and $\dot{\mathbf{q}}(\psi)$, and these are used to compute the modal loads $f_{i,j}$ and $f_{D,i}$. This arrangement is treated in an iterative scheme for which the overall goal is the computation of the steady responses of the untrimmed or trimmed flight, for the specified flight and control conditions. Further details on the code organization and the computational approach are in [34–40].

The force induced by the model of the lag damper is assumed to be proportional to the pressure difference Δp between the two chambers of the damper. The evolution of the state variable Δp will be described by the equations introduced later. Excitation of this model is due to the velocity of the point C, denoted as $\dot{\mathbf{x}}_{AC}$. This velocity is transformed into the damper local coordinate system as $\dot{y}_P(\psi)$. The damper force F_D is then converted to the equivalent blade forces and moments and then projected into the ith modal subspace of the mode shape $\boldsymbol{\varphi}_i$:

$$f_{D,i}(\psi) = \int_{(X)} \boldsymbol{\varphi}_i^T(X)(\mathbf{P}_{EC}\mathbf{t}_{DC}F_D(\psi))\delta(X - X_E)\,\mathrm{d}X$$
$$= (\boldsymbol{\varphi}_i^T(X_E)\mathbf{P}_{EC}\mathbf{t}_{DC})F_D(\psi) \tag{5}$$

where $\delta(\circ)$ is the Dirac delta function, X_E is the normalized position of the damper attachment arm E-C, $\mathbf{t}_{DC} \in \mathbb{R}^{3\times1}$ is the transformation matrix resolving F_D into the directions of the local blade coordinate system while assuming the rigid damper attachment arm, and $\mathbf{P}_{EC} \in \mathbb{R}^{N_D\times3}$ is the static force transfer matrix producing a statically equivalent system of the forces and moments acting on the blade localized at the point E (Fig. 1). This system of equivalent loads is projected in Eq. (5) into the subspace of the mode shape $\boldsymbol{\varphi}_i$, assuming that this mode shape contains a compatible set of degrees of freedom.

III. Computational Platform for Hydraulic, Physically Based, Lag-Damper Models

A. Basic Lag-Damper Modeling Arguments

The lag damper is, in effect, a high-pressure hydraulic device with internal circulation. An example of the measured damper activity (i.e., damper forces and piston velocities) corresponding to four different steady forward-flight regimes acquired during the test flights of a medium-sized production helicopter is presented in Fig. 2.

All four subplots of this figure show the normalized piston velocity versus damper force loops. The normalizing factors for these figures are not available due to their commercially sensitive nature, and this will also be the case in the later case studies. The four subplots of Fig. 2 represent the cases with progressively increasing flight speed, and the direction of travel in these loops is anticlockwise, due to elastic effects in the damper subsystem. All four cases indicate the same characteristic features justifying the chosen modeling methodology. The two primary observations are as follows:

1) The two-stage behavior of the damper shows a rapid increase in force for the small piston velocities and subsequent reduction of the rate of the force increase for large piston velocities.

2) There is a significant delay or hysteresis in the damper's responses. The first effect has a functional origin and the second effect is an inevitable consequence of the use of real materials with finite stiffness of its subsystems, such as the working fluid compressibility, damper cylinder flexibility, etc.

The combination of the functional behavior and the physical effects leads to the requirement to use a fairly detailed modeling methodology if the goal of its implementation is the improved understanding of the physical interactions within its standard operational framework.

B. Generic Platform Implementing Standard Lag-Damper Topology

The organization of the damper is based on the generic topology shown in Fig. 3. The piston rod is connected to the one side of a structure and the cylinder is connected to the second part of the structure. The working chambers contain a hydraulic fluid, and the relative movement of the piston induces the flow of the fluid between

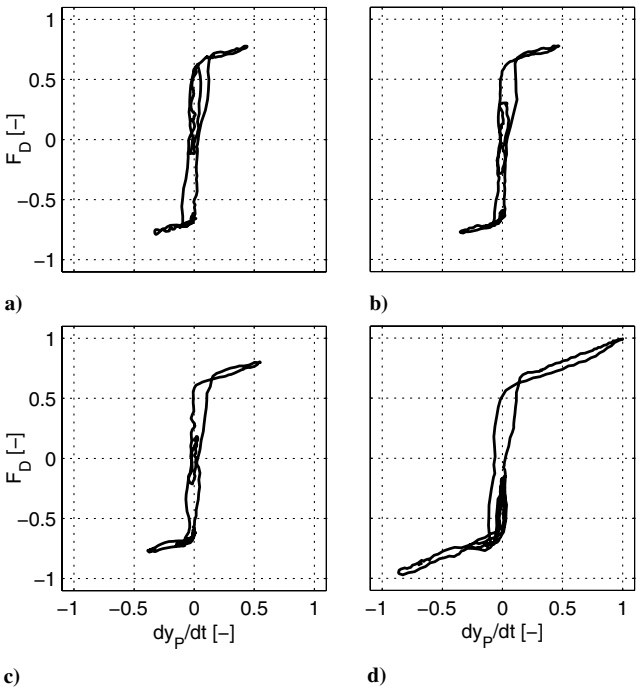

Fig. 2 Normalized velocity-force damper loops for four different steady flight regimes.

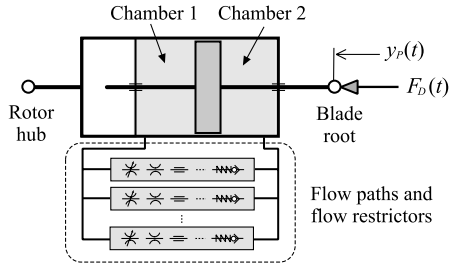

Fig. 3 Hydraulic lag-damper model template with the multiple parallel flow branches with the serial chains of the flow restrictors.

the chambers through the passages located either in the piston or externally, such that the induced dissipative losses in the flowing fluid provide the required characteristics of the damper.

This paper considers the dampers with the symmetric piston rod arrangement due to their relevance with the existing lag-damper implementations. A symmetric arrangement of the piston rod allows the use of the model using a pressure differential $\Delta p = p_1 - p_2$, where p_1 and p_2 are the absolute pressures in the two working chambers. The pressure differential based model was used in [13,16,27].

The model presented in [27] with the associated assumptions is taken as a reference for further specializations. Introduction of the multiple branches with the varying number and types of the flow restrictors in each of them can be represented by the generic hydraulic equation of the damper based on the derivations from [27]

$$\frac{\mathrm{d}(\Delta p)}{\mathrm{d}t} = B_0\left(\frac{1}{V_1(y_P)} + \frac{1}{V_2(y_P)}\right) \times \left[A_P \frac{\mathrm{d}y_P}{\mathrm{d}t} - \sum_{(\pi)} Q_\pi(\Delta p)\right] \quad (6)$$

where B_0 is the constant effective bulk modulus of the fluid, y_P is the displacement of the piston, A_P is the piston cross-sectional area exposed to the fluid, V_1 and V_2 are the variable volumes of the working chambers, and Q_π is the volumetric flow rate through the branch π.

The static part of the model is presented here for the branch π of the damper (Fig. 3). A serial arrangement of the elements in the single branch and the flow continuity is assumed (see [27]). These conditions can be specified as follows:

$$\Delta p = \sum_{(j)} \Delta p_{\pi,j}, \quad Q_\pi = Q_{\pi,1} = \cdots = Q_{\pi,N_\pi} = \mathcal{B}_\pi \tilde{Q}_\pi, \quad \mathcal{B}_\pi \in \{0,1\}$$
$$Q_{\pi,j} = q_{\pi,j}(\Delta p_{\pi,j}), \quad \Delta p_{\pi,j} = q_{\pi,j}^{-1}(Q_{\pi,j}) \quad (7)$$

where the overall pressure difference Δp depends on the pressure losses $\Delta p_{\pi,j}$ caused by the N_π constituent flow-restricting elements; Q_π is the volumetric flow rate through the branch π, and due to its continuity, it is equal to the flow rates $Q_{\pi,j}$ of the constituent flow restrictors; and $q_{\pi,j}$ and $q_{\pi,j}^{-1}$ are the direct static and inverse static characteristics of the jth flow restrictor on the branch π. The flow rate through the branch π can be conditionally dependent on the multiplicator $\mathcal{B}_\pi$ dependent on the problem-specific conditions (e.g., the valve activation [16]).

Equation (7) suggests that for a known overall Δp and fully defined characteristics $q_{\pi,j}^{-1}$, in general, a nonlinear equation can be established in the form

$$\Delta p = \sum_{(j)} q_{\pi,j}^{-1}(Q_\pi)$$

to compute the flow rate Q_π through the branch π and therefore of all its constituent N_π flow restrictors. The knowledge of Q_π can then be used in the separate equations of the type $\Delta p_{\pi,j} = q_{\pi,j}^{-1}(Q_\pi)$ to compute the restrictor specific pressure loss $\Delta p_{\pi,j}$. This process can be applied to all parallel branches of the network interconnecting the chambers of the damper (Fig. 3).

The dynamic part of the damper model represents the generalized balance of the flow rates in Fig. 3, such that

$$Q_P - Q_\beta - \sum_{(\pi)} Q_\pi = 0$$

where $Q_P = A_P \dot{y}_P$ is the flow rate induced by the movement of the piston,

$$Q_\beta = \beta_0 (1/V_1 + 1/V_2)^{-1} \Delta \dot{p}$$

is the effective flow rate due to compressible fluid, and Q_π is the flow rate through π.

The pressure differential is a major component contributing to the overall force produced by the damper. The total damper force is assumed in the form

$$F_D = A_P \Delta p + m_P \ddot{y}_P - \mathrm{sign}(\dot{y}_P)|F_f| \approx A_P \Delta p$$

where F_f is the friction force and m_P is the mass of the piston. Inclusion of other physical effects can be relevant in some scenarios. However, the architecture presented in Fig. 3 is assumed to be sufficient for the steady-state configuration described in Sec. II.

An example of the previously described concepts is shown in Fig. 4. The figure shows the nominal model of the lag damper investigated in [13,15]. The presence of the lines with the relief valves requires a qualitative augmentation of the standard hydraulic part of the model [Eqs. (6) and (7)] by the additional mechanical states.

The configuration shown in Fig. 4 leads to the following flow rate transported between the working chambers:

$$\sum_{(\pi)} \mathcal{B}_\pi \tilde{Q}_\pi = \mathcal{B}_O \tilde{Q}_O + \mathcal{B}_1(x_{V,1}, \Delta p)\tilde{Q}_{V,1} + \mathcal{B}_2(x_{V,2}, \Delta p)\tilde{Q}_{V,2}$$
$$\mathcal{B}_O = 1, \qquad \mathcal{B}_1 \in \{0,1\}, \qquad \mathcal{B}_2 \in \{0,1\} \quad (8)$$

where $\tilde{Q}_{V,1}$ and $\tilde{Q}_{V,2}$ are the flow rates through the relief valves. The coefficients $\mathcal{B}_1$ and $\mathcal{B}_2$ indicate the conditional nature of the corresponding flow terms.

The relief valves can be modeled as discrete subsystems with a single mechanical degree of freedom (DOF) for each relief valve, with direct coupling with the hydraulic domain in the form of the external excitation. A single-DOF oscillator in a preloaded state can represent a relief valve. This concept was used by Hayashi et al. [33] and it is used here in the following form:

$$\mathrm{d}\dot{x}_V/\mathrm{d}t = (F_{\mathrm{hydro}} - b_V \dot{x}_V - k_V(x_V \mp X_C))/m_V$$
$$F_{\mathrm{hydro}}(t) = \Delta p A_V \{1 - 4C_{D,V,0}[\gamma|x_V|/(1+\gamma|x_V|)] \times (|x_V|/d_V)\sin(2\alpha)\} \quad (9)$$

where x_V is the displacement of the relief-valve poppet, and $X_C = \Delta P_C A_V / k_V$ is the equivalent displacement corresponding the critical pressure differential ΔP_C. Parameters m_V, b_V, and k_V represent, respectively, the effective mass, damping, and stiffness of the 1-DOF valve oscillator. $A_V = \pi d_V^2/4$ is the cross-sectional area of the valve-seat aperture. F_{hydro} is the model of the hydraulic excitation force induced by the pressure differential across the valve, $C_{D,V,0}$ and γ are the estimated coefficients of the asymptotic model of the discharge coefficient, and α is the half-angle of the conically shaped valve's poppet.

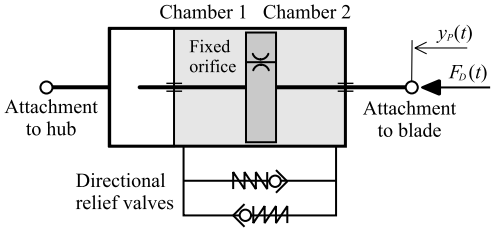

Fig. 4 Specific realization of the lag damper with the relief valves on the bypass routes [13].

The plus–minus sign in Eq. (9) is indicative of the orientation of the coordinate system, such that the relief valve can move in the corresponding direction while being constrained to not move in the other direction. This effect necessitates the use of a model of a variable structure with the conditional events. An assumption of the relatively low operational piston-excitation frequencies results in regimes where either one or none of the relief valves are activated (for more detail, see [14]). In this case, the model according to Fig. 4 has to cover the three possible structural cases:

1) For structural case $\mathbf{f}_1$, $\mathcal{B}_1 = 1$ and $\mathcal{B}_2 = 0$ if $x_{V,1} < 0$ or $\Delta p \leq -\Delta P_C$.

2) For structural case $\mathbf{f}_2$, $\mathcal{B}_1 = 0$ and $\mathcal{B}_2 = 1$ if $x_{V,2} > 0$ or $\Delta p \geq \Delta P_C$.

3) For structural case $\mathbf{f}_3$, $\mathcal{B}_1 = 0$ and $\mathcal{B}_2 = 0$ if $|x_{V,j}| = 0$ and $|\Delta p| \leq \Delta P_C$ for $j = 1, 2$.

As the damper model based on Fig. 4 has two relief valves, its final state-space description can be represented such that each relief valve introduces a pair of the mechanical states $\mathbf{x}_{V,i}^T = [x_{V,i}, \dot{x}_{V,i}]$ with the overall state vector:

$$\mathbf{x}^T = [\Delta p, x_{V,1}, \dot{x}_{V,1}, x_{V,2}, \dot{x}_{V,2}] \in \mathbb{R}^5$$

The event-based damper model can be represented as $\dot{\mathbf{x}} = \{\mathbf{f}_1, \mathbf{f}_2, \mathbf{f}_3\}$ with the individual models $\mathbf{f}_i = \mathbf{f}_i(t, \mathbf{x}; \mathbf{p})$, where $\mathbf{p} \in \mathbb{R}^{N_P}$ is the vector of physical parameters of the damper and N_P is the total number of these parameters.

C. Three Specializations Based on the Generic Damper Description

Based on the previous discussion, the three alternative lag-damper model representations are demonstrated in Fig. 5. These are the specializations of the generic model shown in Fig. 3.

1. *Baseline Lag-Damper Model*

The lag-damper model shown in Fig. 5a was developed by Eyres [15]. This model is the specialization of the model (6) and (7), assuming small piston oscillations around the reference position and that $V_2 = \zeta V_1 = \text{const}$ ($\zeta > 0$). The flow rate term $\sum_{(\pi)} Q_\pi$ is assumed with a single effective valve term, leading to the following equation:

$$\frac{\mathrm{d}(\Delta p)}{\mathrm{d}t} = \frac{1+\zeta}{\beta_0 V_1 \zeta}[A_P \dot{y}_P - \text{sign}(\Delta p)(Q_O(\Delta p) + \mathcal{B}(\Delta p, x_V) Q_V(|\Delta p|, |x_V|))] \tag{10}$$

where the valve-activation coefficient $\mathcal{B} \in \{-1, 0, 1\}$ represents the flow rate status defined on the basis of the conditions similar to those specified previously for $\mathcal{B}_1$ and $\mathcal{B}_2$ (see [15]), and the flow rate Q_V is defined here such that $Q_V \geq 0$. The nominal constant of the fluid compressibility $\beta_0 = 1/B_0$ was used in [13–15].

2. *Refined Baseline or Extended Lag-Damper Model*

The damper model shown in Fig. 5b demonstrates the model after its refinement based on the experimental investigation described in [16]. Within this work, an effective fluid compressibility β_0^* was assumed. The model configuration proposed in [16] introduced the secondary bypass orifices, together with an updated model of the relief valve. The hydraulic state equation has then the form

$$\frac{\mathrm{d}(\Delta p)}{\mathrm{d}t} = \frac{1+\zeta}{\beta_0^* V_1 \zeta}[A_P \dot{y}_P - \text{sign}(\Delta p)(Q_O(\Delta p) + \mathcal{B}(\Delta p, x_V) Q_V^*(|\Delta p|, |x_V|))] \tag{11}$$

where an improved understanding of the pressure-loss mechanisms can be applied to compute refined values of the flow rate Q_V^*. The new composite static characteristic is

$$Q_V^*(\Delta p, x_V) = \text{sign}(\Delta p) K_V^*(x_V) \sqrt{2|\Delta p|/\rho},$$
$$K_V^*(x_V) = \{1/(C_{D,V}^2(x_V) A_{V,\text{eff}}^2(x_V)) + 1/(C_{D,V,O}^2 A_{V,O}^2)\}^{-1/2} \tag{12}$$

where $C_{D,V}$ is the discharge coefficient of the variable orifice, as defined in [33]; $A_{V,\text{eff}}$ is the effective valve area freed by the moving valve's poppet [33]; $C_{D,V,O}$ is the discharge coefficient of the secondary orifice on the bypass route placed in the series with the relief-valve model; and $A_{V,O}$ is the effective secondary orifice area.

In the case of the study presented in [16] the characteristic (12) assumes the presence of the secondary orifice features located on the bypass route. These are physically associated with a parallel arrangement of the relief-valve sleeve holes, which are placed in series with the valve orifice. The corresponding flow rate continuity condition can be written as

$$Q_V^* = Q_{V,1}^* = Q_{V,2}^* = \sum_{(j)} Q_{V,j,O}^*$$

where $Q_{V,1}^*$ is the flow rate through the relief valve, $Q_{V,2}^*$ is the total flow rate through the secondary bypass orifice, and $Q_{V,j,O}^*$ is the flow rate through a single sleeve hole. Introduction of the additional flow restrictor causes a pressure differential redistribution across these two features, $\Delta p = \Delta p_V + \Delta p_{V,O}$, where Δp_V are the pressure losses across the relief valve and $\Delta p_{V,O}$ are the pressure losses across the secondary bypass orifice. This modification alters also the hydromechanical coupling represented by Eq. (9), where $F_{\text{hydro}} = F_{\text{hydro}}(x_V, \Delta p_V)$ [16].

3. *Semi-Active Mode of the Damper Operation*

The damper model with an active or variable-flow restrictor is shown in Fig. 5c. It is based on the work presented in Titurus and Lieven [27]. In this case, the flow rate component $\sum_{(\pi)} Q_\pi$ of Eq. (6) consists of a single flow rate term $Q_A(\Delta p, u(t))$ corresponding to the flow through the flow restrictor with controllable geometry. Adopting a simplified modeling methodology for this type of the device (e.g., [1–3,21,22]), a simple semi-analytical model of the controllable flow restrictor can be based on the orifice static characteristics with a flow area parameter A_A dependent on the control input $u(t)$. The equation of the damper is then as follows [27]:

$$\frac{\mathrm{d}(\Delta p)}{\mathrm{d}t} = B_0 \left(\frac{1}{V_1(y_P)} + \frac{1}{V_2(y_P)}\right) \times \left[A_P \frac{\mathrm{d}y_P}{\mathrm{d}t} - \text{sign}(\Delta p) C_{D,A} A_A(u(t)) \sqrt{(2/\rho)|\Delta p|}\right] \tag{13}$$

where $A_A = A_A(u(t))$ is the effective cross section defined analytically or via a lookup table, and it is based on experimentally determined characteristics, also accounting for the qualitative flow changes.

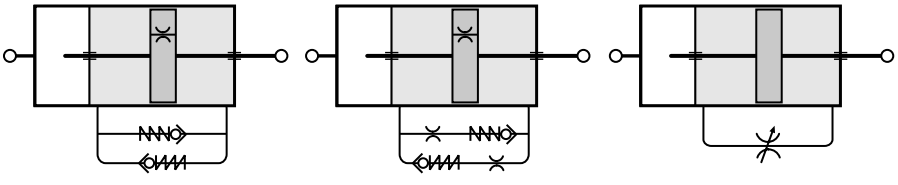

a) b) c)

Fig. 5 Examples of alternative damper models based on the generic model template: a) baseline damper model, b) refined baseline damper model, and c) semi-active damper model.

IV. Coupled Rotor–Damper Computational Framework

The coupled rotor–damper platform with the proposed damper model organization is described in Fig. 6. The original R150 rotor code implements the dynamics of a rotating elastic blade in an aerodynamic environment. The damper code models the damper's internal hydromechanical behavior. Figure 6 also outlines the method of the interaction between these two code blocks.

The nominal part of the code R150, as shown in Fig. 6, implements the forward trimmed flight computations. The two inner loops provide the rotor-blade–azimuth integration capability. The computations of the aerodynamic and inertial loads are complemented with a damper load computation performed for each azimuth step ψ_j, where $j = 1, \ldots, N_\psi$ and $N_\psi \Delta\psi = 2\pi$. This is also indicated in Eq. (4), where the modal loads of the ith blade mode shape $\boldsymbol{\varphi}_i$ are formulated as

$$\mathrm{ML}_i = \sum_{(j)} f_{i,j}(\mathbf{q}, \dot{\mathbf{q}}) + f_{D,i}(\mathbf{q}, \dot{\mathbf{q}})$$

where $\mathbf{q} = \mathbf{q}(\psi)$, $\dot{\mathbf{q}} = \dot{\mathbf{q}}(\psi)$, and the ith damper modal force $f_{D,i}$ is introduced in Eq. (5).

The four modules within the lag-damper section of Fig. 6 implement the following:

1) The damper equation solution method within the azimuth step $\Delta\psi$ includes the representation of the kinematic relationships (1) and (2), the physical coupling between the rotor and the damper domains, the processing of the damper states $\mathbf{x}(\tau)$ for the interval $\tau \in [\psi_k, \psi_{k+1}]$ to compute $F_D(\psi_{k+1})$, and the computation of $f_{D,i}(\psi_{k+1})$ based on Eq. (5).

2) The specific form of the state equations of the damper $\dot{\mathbf{x}} = \{\mathbf{f}_U\}$ with the index set U of the all operational configurations depend on the selected functionality, and it is based on the theory presented in Sec. III.

3) The characteristics of the rth flow restrictor $Q_r = q_r(\Delta p_r, \mathbf{p}_r)$ [e.g., $Q_A(\Delta p, u(t))$ in Eq. (13)] is parameterized with the vector of the physical restrictor parameters $\mathbf{p}_r \in \mathbb{R}^{N_r}$.

4) The optional block allows the active signal parameterization [27]

$$\mathbf{p}_{r,\mathrm{act}} = \mathbf{p}_{r,\mathrm{act}}(\psi, \mathbf{p}_{r,A}) \in \mathbb{R}^{N_{r,\mathrm{act}}}$$

where $\mathbf{p}_{r,\mathrm{act}} \subset \mathbf{p}_r$, $N_{r,\mathrm{act}} \leq N_r$, and $\mathbf{p}_{r,A} \in \mathbb{R}^{N_{r,A}}$ is the vector of activity parameters.

The arrangement shown in Fig. 6 is used to compute the steady-state flight regimes. The trimmed flight is computed during a sequence of modal convergence scenarios characterized by the repeated patterns of the modal displacement waveforms at the selected azimuth positions $\psi_k \in [0, 2\pi]$ for the two subsequent azimuth cycles. The modal displacements are denoted as $\mathbf{q}^{(n)}(\psi_k)$ and $\mathbf{q}^{(n-1)}(\psi_k)$, and the criterion of periodicity is as follows [34]:

$$\left| \left(\sum_{i=1}^{N_m} |q_i^{(n)}(\psi_k)| \Big/ \sum_{i=1}^{N_m} |q_i^{(n-1)}(\psi_k)| \right) - 1 \right| \leq \Delta_q, \quad k = 1, 2, \ldots, N_\psi \tag{14}$$

where Δ_q is the modal displacement convergence threshold.

The sequence of modal convergence scenarios is driven such that specific trim flight requirements are fulfilled. These are specified in the form of predetermined flight control and performance parameters (e.g., prescribed blade flapping and total rotor thrust, pitching control, etc.). Because of the assumption of the steady-state flight conditions, Eq. (4) is solved with the provided Z-transform-based method or with the harmonic balance method [34]. The work presented in this paper deals exclusively with damper-related elements of the configuration shown in Fig. 6. Computationally expensive studies require further algorithmic optimization of the simulation environment. This is achieved via the serial staggered scheme with damper subiterations or the (damper) subcycling [30–32].

An interaction between the rotor and damper models can be characterized by the total number of rotor steps per one rotor revolution $N_{\mathrm{rotor}} = N_\psi$ and by the number of the damper internal steps per one rotor step, denoted as N_{damper}. The following notation will be used to denote the rotor–damper simulation arrangement N_{rotor}:N_{damper}.

The baseline implementation of a passive lag-damper model presented in [15] used coupling mode N_{rotor}:1. Eyres [15] dealt with a passive hydraulic lag damper equipped with the relief valves (Fig. 5a). The computational scheme 3600:1 with $\Delta\psi = 0.1°$ was applied throughout those studies. The choice of this specific damper integration interval, $\Delta\psi = 0.1°$, was performed on the basis of a dedicated convergence study. This discretization was found to be necessary to assure numerical stability of the integration scheme N_{rotor}:1. The fourth-order Runge–Kutta time-stepping method was used to compute the damper states at ψ_{k+1} and $\psi_k + \Delta\psi/2$. The new damper state $\mathbf{x}(\psi_{k+1})$ was derived from its previous state $\mathbf{x}(\psi_k)$, assuming $\dot{y}_P(\psi_k)$ computed from the blade velocity state based on Eq. (3) at the azimuth ψ_k and with the help of the relationships (1) and (2). In the studies presented in [15], the coupling structure of the code was adjusted to the most critical response timescale, which was due to damper internal dynamics, resulting in a relatively computationally inefficient N_{rotor}:1 scheme. An alternative, the subcycling approach (e.g., [30]) is applied in this work, as indicated in Fig. 6. An effort here is to reduce N_{rotor} while $N_{\mathrm{damper}} > 1$. This arrangement is shown in Fig. 6 as the loop with the damper subcycles, where $\Delta\psi = 2\pi/N_{\mathrm{rotor}}$ is divided into the substeps $\Delta\psi_{\mathrm{dmp}} = \Delta\psi/N_{\mathrm{damper}}$. In the present helicopter case study, the scheme N_{rotor}:N_{damper} will be

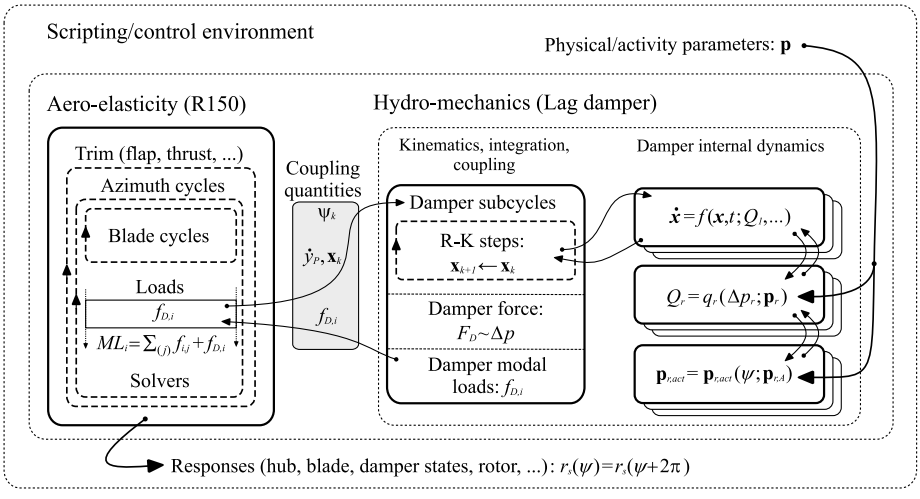

Fig. 6 Modules used to provide extended platform with hydraulic lag-damper model.

chosen such that $N_{\text{damper}} > 1$ and $\Delta\psi_{\text{dmp}} = 0.1°$ according to the recommendation from [15].

The damper behavior [e.g., Eq. (6)] is evolving in the interval $[\psi_k, \psi_{k+1}]$, starting from the state $\mathbf{x}(\psi_k)$, assuming piston excitation $\dot{y}_P(\psi_k)$ derived from $\mathbf{q}(\psi_k)$ and $\dot{\mathbf{q}}(\psi_k)$ [e.g., Eq. (3)] and further assuming constant $\dot{\mathbf{q}}(\psi)$ for $\psi \in [\psi_k, \psi_{k+1}]$. The fourth-order Runge–Kutta method evolves states within the interval $[\psi_k, \psi_{k+1}]$, and $\Delta p(\psi) = x_1(\psi)$ for $\psi \in [\psi_k, \psi_{k+1}]$ is used to compute the force $F_D(\psi_{k+1})$ with the same work done as the work due to the force $F_D(\tau)$ for $\tau \in [\psi_k, \psi_{k+1}]$; that is,

$$F_D(\psi_{k+1}) = \int_{\psi_k}^{\psi_{k+1}} F_D(\psi)\,\mathrm{d}y_P(\psi) \Big/ \int_{\psi_k}^{\psi_{k+1}} \mathrm{d}y_P(\psi)$$

The damper force $F_D(\psi_{k+1})$ is then used in Eq. (5) to produce the modal damper forces $f_{D,i}(\psi_{k+1})$ $(i = 1, \ldots, N_m)$, and these are used later in the rotor code to assemble the total modal load ML_i, as indicated in Eq. (4) by the term in parentheses.

V. Case Studies

Two case studies are presented in this section. The first study illustrates the capability of the damper model to exhibit improved predictive behavior using the knowledge derived from the experimental data. The second study demonstrates the use of the coupled rotor–damper simulation code R150 for a physically based conceptual study of the semi-active lag damper and its capacity to alter nominal rotor behavior.

The significance of the first study lies in the fact that the existing device for which the model can be validated and evaluated in the laboratory conditions is later redefined to the semi-active mode of operation (Fig. 5c) and then used in the second concept study. This soft model transformation is achieved by the parameterization of the flow-restrictor opening $A_A(u)$ and by setting the relief-valve opening pressure differentials ΔP_C to the higher values to avoid their activation during corresponding studies. The softness of this process relates to the fact that the alterations applied to the validated model are not structural (i.e., the model structure is retained). These damper model changes represent technologically feasible modifications where the change of ΔP_C is simply achievable by the change of the relief-valve precompression and the parameterization of $A_A(u)$ can be achieved in practice with a controllable flow restrictor (e.g., [21,22]). The latter modification is based on the standard methods of flow control used for hydraulic actuators. As both hydraulic dampers and actuators are exposed to similar hydromechanical conditions, the damper modeling concepts presented in Sec. III for use at this concept development stage are consistent with those employed for hydraulic actuators (e.g., [1–3,21,22]).

In the rotor–damper simulation case, a steady trimmed forward flight of a medium-sized production helicopter is assumed. The main rotor consists of five blades in a fully articulated arrangement with the lag dampers, according to the scheme outlined in Fig. 1. The responses are computed for trimmed flight with the prescribed rotor thrust vector and blade flapping. In the cases of the helicopter studies, a full-complexity trimmed steady-state forward flight is assumed. The structural model of the blades is constituted by its modal representation based on the first eight coupled flap-lag-pitch normal modes, covering the frequency range up to approximately $13R$. The structural and the aerodynamic specification of the blades is based on the same production helicopter with its fully articulated five-bladed main rotor. The aerodynamic part of the rotor model is based on the experimental airfoil characteristics employing the near-wake mode with the far-field vortex-ring model for the blade-related induced-velocity distribution and the slender-body theory for the fuselage induced-velocity field. The Beddoes–Leishman model is used to take account of unsteady aerodynamic effects.

A. Demonstration of Refined Damper Model Performance

This case study demonstrates the results of the lag-damper model refinement effort. Titurus and Lieven [16] investigated the lag-damper model proposed by Eyres et al. [13] and the possibility for its further refinement. The model refinement study documents the potential of the modeling methodology to provide improved load predictions for the passive mode of the damper. The success and, particularly, the failure in the refinement study could have further implications for the semi-active damper modeling, as the semi-active damper can be seen as the functional extension of the passive case. In the study [16], the predicted damper forces are compared with the experimentally measured damper forces. The prescribed piston displacement is $1R$ sine excitation. Two sets of data are selected here from 12 excitation cases considered in [16], and these are presented in Fig. 7. The correlation and refinement studies were based on the comparison of the responses generated by the reference model (9) and (10) and the refined model (11) and (12) with the equivalent experimental data. The data are presented in the normalized format in which the normalization in all cases is based on the maxima of the corresponding experimental data. The gray thick lines represent experimental data, and the thin black lines represent results from individual damper simulations.

The first row of Figs. 7a and 7b represents the initial correlation based on the reference or baseline model. Both characteristics, the displacement force and the velocity force, indicate good correspondence between the experimental and the simulation responses. However, qualitative difference is observed in the high-piston-velocity regions, where the model provides increasingly underestimated predictions of the damper forces. This qualitative difference is considered to be an important element to address. An inspection of the damper construction and the damper model structure [e.g., Eq. (6)] allows model refinement based on the identified additional pressure-loss features located on the bypass route [16]. The pressure-loss features are implemented as the additional flow restrictors located on both relief-valve flowpaths, assuming a purely turbulent pressure-loss mechanism. These modifications are summarized in Eqs. (11) and (12). The resulting modified responses due to the refined model are shown in Figs. 7c and 7d. The newly added features indicated in Fig. 5b lead to the improved qualitative prediction of the damper forces. Considering the modifications described in the previous section, this model, coupled with the helicopter rotor model, constitutes the basis for the investigations presented in the following case study.

B. Demonstration of the Semi-Active Lag-Damper Concept

The purpose of this study is the demonstration of the capabilities associated with the use of the lag damper with active modulation of its internal physical parameters. The model of the damper is based on Eq. (13) and is shown in Fig. 5c. A steady trimmed forward flight is

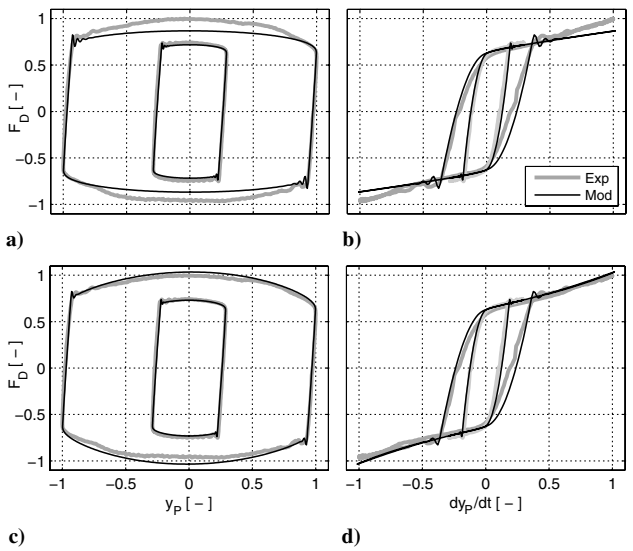

Fig. 7 Lag-damper model correlation with the experimental characteristics (thin black lines: simulated responses, thick gray lines: damper experimental data).

assumed with a speed of 149 kt. A harmonic parameterization of the active signal is chosen at the frequency $3R$, and the normalized parameter activity of the flow-restrictor opening is as follows, assuming

$$A_A(\psi) = \varepsilon_V x_{V,\text{norm}}(\psi)$$

where ε_V is the scaling constant,

$$\begin{aligned} x_{V,\text{norm}}(\psi) &= 1 + \bar{p}_1 \cos(3\psi) + \bar{p}_2 \sin(3\psi) \\ \mathbf{p} &= \mathbf{p}_{\text{act}} = \mathbf{p}_{1,\text{act}} = [x_{V,\text{norm}}] \in \mathbb{R}^1 \\ \mathbf{p}_A &= \mathbf{p}_{1,A} = [\bar{p}_1, \bar{p}_2] \in \mathcal{D}_P \subset \mathbb{R}^2 \end{aligned} \tag{15}$$

This form of damper activity generates the feasible parameter domain $\mathcal{D}_P \subset \mathbb{R}^2$, where a pair of the harmonic parameters $[\bar{p}_1, \bar{p}_2]$ is chosen such that it provides a physically feasible restrictor opening. This is defined such that

$$x_{V,\text{norm}}(\psi) \geq x_{V,\text{MIN}} > 0$$

for $\psi \in [0, 2\pi]$, where $x_{V,\text{MIN}}$ represents the minimal acceptable opening of the restrictor, and $x^*_{V,\text{MIN}} = 0$ represents the singular case with instantaneously blocked fluid flow. For the current demonstration, the value $x_{V,\text{MIN}} = 0.12$ is chosen to avoid the loss of stability of the $R150$ code during the convergence process, due to excessively high damper forces. Domain $\mathcal{D}_P$ is a circular domain with radius equal to 1 in the case of $x^*_{V,\text{MIN}} = 0$. An assumption of $x_{V,\text{MIN}} > 0$ reduces the radius of $\mathcal{D}_P$, and its center remains at the point $\mathbf{p}_A = [0, 0]$.

A constrained parametric analysis in $\mathcal{D}_P \subset \mathbb{R}^2$ is presented in this section. The main action of the damper, due to its localization in the rotor system, can be expected in the rotor plane. As a result of the parameterization in Eq. (15), the six nonrotating hub forces and moments introduced in Sec. II (i.e., F_X, F_Y, F_Z, M_X, M_Y, and M_Z) are considered to be functions of $\mathbf{p}_A$ in $\mathcal{D}_P$. Further, the cost function $J_{XY}(\mathbf{p}_A)$, based on the rotor in-plane force components, is considered in the form

$$J_{XY} = \sqrt{(F^2_{X,\cos} + F^2_{X,\sin} + F^2_{Y,\cos} + F^2_{Y,\sin})} \tag{16}$$

where $F_{X,\cos}, F_{X,\sin}, F_{Y,\cos}$, and $F_{Y,\sin}$ are the harmonic components of nonrotating $5R$ rotor-hub in-plane forces.

This quantity will be qualitatively compared with other hub and rotor responses to enable the investigation of the semi-active damper mode of operation. All quantities presented here will be normalized with respect to the passive damper configuration; that is,

$$R_N(\mathbf{p}_A) = \frac{R(\mathbf{p}_A)}{R(\mathbf{0})}$$

where R represents any considered quantity (e.g., load component or cost function).

$R(\mathbf{0})$ represents the reference value corresponding to the passive regime of damper operation with $\mathbf{p}_A = [0, 0]$ (i.e., the damper with all physical parameters unperturbed).

Figure 8 provides an overall picture of the system response with respect to the cost function $J_{XY}(\mathbf{p}_A)$ specified on $\mathcal{D}_P \subset \mathbb{R}^2$. This study is constituted by the regular grid of 17×17 test points $\mathbf{p}^*_A$ specified on the square domain $[-1, 1] \times [-1, 1]$. Only those test points are accepted for the further parametric runs where $\mathbf{p}_A = \mathbf{p}^*_A \in \mathcal{D}_P$, and $\mathcal{D}_P$ is established by selecting $x_{V,\text{MIN}} = 0.12$. Accepted test points are shown in Fig. 8 as gray points located at the level $J_{XY} = 0$. Furthermore, the solid circle in this figure represents parameter configurations $[\bar{p}_1, \bar{p}_2]$ that would lead to the instances of the damper with instantaneously blocked fluid flow, and the dashed circle denotes the selected $\mathcal{D}_P$. Two solid contours intersecting the points [0, 0, 0] and $[0, 0, J_{XY}(\mathbf{0})]$ represent the condition in which $J_{XY}(\mathbf{p}^{(0)}_A) = 1$ (i.e., the boundary between improved and reduced performance as defined in terms of the function J_{XY}). The circle marker located on the surface of the function represents the nominal inactive case with $\mathbf{p}_A = [0, 0]$ and $x_{V,\text{norm}}(\psi) = 1$ for all $\psi \in [0, 2\pi]$.

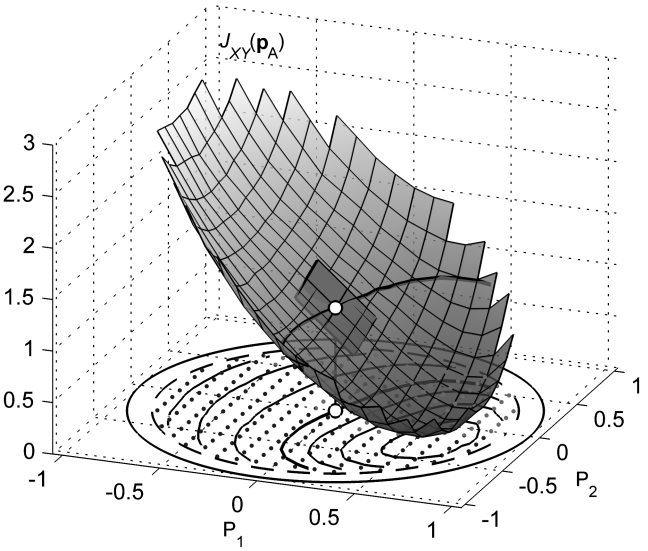

Fig. 8 Cost-function surface for parametric study with $3R$ flow-restrictor activity.

Finally, the gray plane represents the tangent plane $\mathcal{T}$ to the cost-function surface at the point $\mathbf{p}_A = [0, 0]$. The derivatives specifying $\mathcal{T}$ are

$$\frac{\partial J_{XY}(\mathbf{0})}{\partial \mathbf{p}_A} = 2\mathbf{T}^T \mathbf{z}_R(\mathbf{0})$$

where

$$\mathbf{T} = \frac{\partial z_{R,i}}{\partial \bar{p}_i} \in \mathbb{R}^{4\times 2}$$

is the response sensitivity matrix,

$$\mathbf{z}_R = [F_{X,\cos}, F_{X,\sin}, F_{Y,\cos}, F_{Y,\sin}]^T \in \mathbb{R}^4$$

is the vector of model responses, and $J_{XY} = (\mathbf{z}^T_R \mathbf{z}_R)^{1/2}$. These quantities allow construction of the linearized and quasi-static model [25] of this problem, specified as follows:

$$\mathbf{z}_R(\mathbf{p}_A) \approx \mathbf{z}_R(\mathbf{0}) + \mathbf{T}\mathbf{p}_A$$

The plane $\mathcal{T}(\mathbf{0})$ provides an indication of possible consequences and potential problems associated with global or local linear approximations, encountered in efforts to reach the global optimum of even this relatively simple problem [24]. Figure 8 provides an indication of the existence of a single minimum in $\mathcal{D}_P$ as well as the extent of the reduction in the cost-function value, where

$$\min(J_{XY}(\mathcal{D}_P)) \approx 0.1$$

The point $\mathbf{p}_{A,\text{opt}}$ can be identified relatively close to the boundary of $\mathcal{D}_P$, which indicates significant activity of the flow restrictor and possibly large peaks in the local damper force $F_D(\psi)$ for $\psi \in [0, 2\pi]$, due to an instantaneously small opening of the flow restrictor. Another observation associated with this figure is related to the possible effort to automate the process of finding $\mathbf{p}_{A,\text{opt}}$. It is obvious that, as a minimum, parameter-based constraints would have to be introduced to retain the algorithm's parameter search within $\mathcal{D}_P$, both for physical and computational reasons.

The previous figure is complemented with Fig. 9. This figure demonstrates the influence of the semi-active damper operation on the peak damper forces:

$$F_{D,\text{peak}}(\mathbf{p}_A) = \max(\text{abs}(F_D(\psi; \mathbf{p}_A)))$$

where $\psi \in [0, 2\pi]$ and $\mathbf{p}_A \in \mathcal{D}_P$. The solid contour lines of the cost function $J_{XY}(\mathbf{p}_A)$ are accompanied here with the dotted contour lines of the function $F_{D,\text{peak}}(\mathbf{p}_A)$, which is normalized with respect

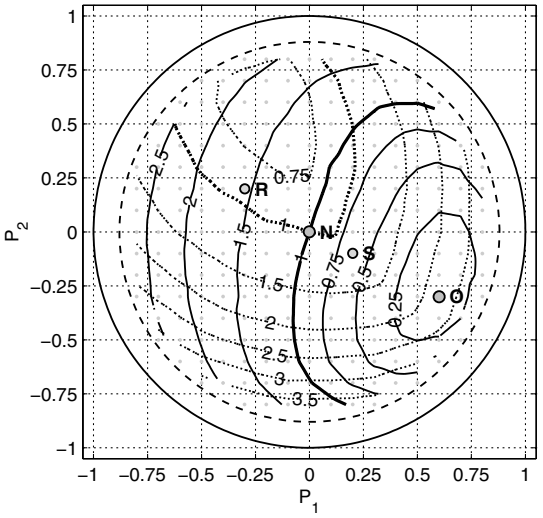

Fig. 9 Effect of parameter modulation on the rotor responses (149 kt): solid lines: cost-function contours, dotted lines: peak damper force contours.

$F_{D,\text{peak}}(\mathbf{0})$. Moreover, this figure contains the selection of four test points that will be used later in a more localized analysis. Selected points are denoted as **O** representing the assumed optimal case in $\mathcal{D}_P$, **S** representing the assumed suboptimal case in $\mathcal{D}_P$, **N** representing the nominal, passive or inactive case in $\mathcal{D}_P$, and **R** representing the assumed case with reduced performance in $\mathcal{D}_P$. Both circular boundaries have an identical meaning to those specified in Fig. 8. The gray points in the dashed circular domain $\mathcal{D}_P$ represent points at which the computations were performed.

Two groups of the contour lines presented in Fig. 9 clearly indicate the tradeoff between the reduction of J_{XY} and increase in $F_{D,\text{peak}}$. The case of the flow-restrictor activity corresponding to the point **O** leads to the increase of the peak damper force $F_{D,\text{peak}}(\mathbf{p}_{A,O}) \approx 2.2$. The search for a global minimum $\mathbf{p}_{A,\text{opt}}$ in $\mathcal{D}_P$ can provide a damper regime, with the peak forces being unfeasibly high. Selection of a suboptimal operating point can be considered as a possible alternative. For the purposes of the present study, an arbitrary test point **S** is selected in the region between the points **O** and **N**. This suboptimal point could represent a solution of the optimization problem with the additional constraint imposed on $F_{D,\text{peak}}(\mathbf{p}_A)$. The current configuration of our problem would thus require $F_{D,\text{peak}}(\mathbf{p}_A) \leq 1.14$, which would generate an associated feasible domain $\mathbf{p}_A \in \mathcal{D}_{FD}$. The overall search domain would be represented as $\mathcal{D}_{P,FD} = \mathcal{D}_{FD} \cap \mathcal{D}_P$ and the constrained solution at the point **O** would be $J_{XY}(\mathbf{p}_{A,S}) \approx 0.62$. The opposite effect is illustrated by the selection of the point **R**, where $J_{XY}(\mathbf{p}_{A,R}) \approx 1.55$ and $F_{D,\text{peak}}(\mathbf{p}_{A,O}) \approx 0.92$. Finally, Fig. 9 indicates that there exists a domain where no tradeoff is required: that is, $J_{XY}(\mathbf{p}_A) < 1.0$ and $F_{D,\text{peak}}(\mathbf{p}_A) \leq 1.0$.

Figure 9 indicates that the consideration of only two rotor response quantities requires a treatment that employs both parameter and response constraints. To conclude this part of the parametric study, Fig. 10 provides an outline of the remaining hub responses in the form of the variation of their magnitudes based on the following generic formula:

$$|R_i| = (R_{i,\cos}^2 + R_{i,\sin}^2)^{1/2}$$

where $R_{i,\cos}$ and $R_{i,\sin}$ are $5R$ cosine and sine components of the hub load responses, respectively. Further, $|R_i(\mathbf{p}_A)|$ is normalized with respect to its nominal value $|R_i(\mathbf{0})|$. In the case of each subplot of Fig. 10, a single response is shown as indicated. The normalized values corresponding to the contours span the same range as in the previous cases (i.e., [0, 3.5]). The investigated quantities are shown as dotted contour lines, and the reference J_{XY} solid contour lines are identical to those shown in Fig. 9.

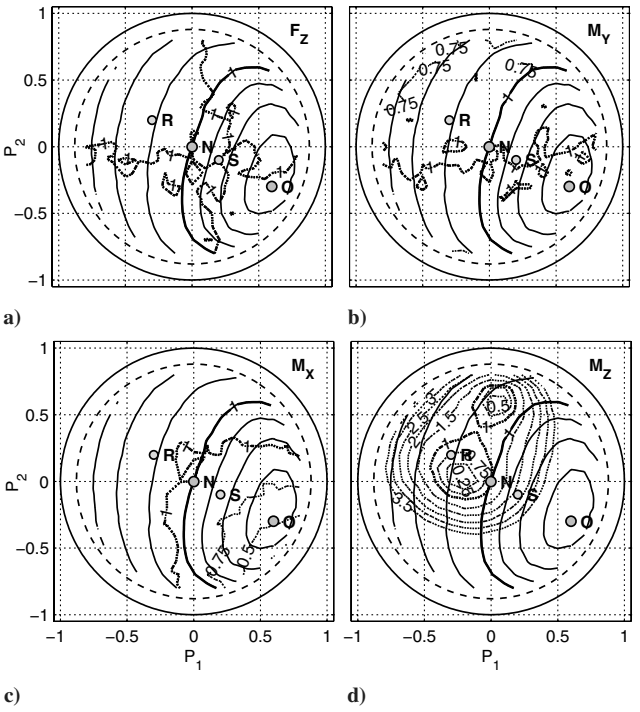

Fig. 10 Effect of damper parameter modulation on the rotor-hub responses: a) vertical $5R$ hub force, b) $5R$ M_Y hub moment, c) $5R$ M_X hub moment, and d) $5R$ M_Z hub moment.

As can be seen in Figs. 10a–10c, the hub responses F_Z, M_X, and M_Y are relatively insensitive to the damper semi-active operation. This is because of the way in which the damper influences the dynamics of the blades, as it acts primarily in the plane of the rotor. However, the quantity that is significantly influenced by the damper activity is the $5R$ nonrotating M_Z hub moment. Considerable sensitivity of this quantity is illustrated by the steep variation of its magnitude in $\mathcal{D}_P$. The magnitude of M_Z rises significantly when moving from case **N** to case **S**, where $|M_Z(\mathbf{p}_{A,S})| \approx 2.16$, and to case **O**, where $|M_Z(\mathbf{p}_{A,O})| \approx 8.1$. Therefore, the moment M_Z represents a further candidate for the response constraint to ensure a structurally feasible solution. Furthermore, Fig. 10d indicates the presence of the two local minima for this quantity, leading to a generally nonconvex and disjoint feasible region.

The previous analysis can be further developed in the more localized context, which is provided in Fig. 11 and 12. The normalized magnitudes of the hub response quantities corresponding to cases **O**, **S**, **N**, and **R** are presented in Fig. 11. In the previous cases, these quantities were normalized with respect to their values computed at $\mathbf{p}_A = [0, 0]$. In the case presented here, the force and the moment quantities are normalized within their respective groups. In both cases, the quantity defined for case **N** and the axis X is used as the reference. Although this leads to the generally different numeric

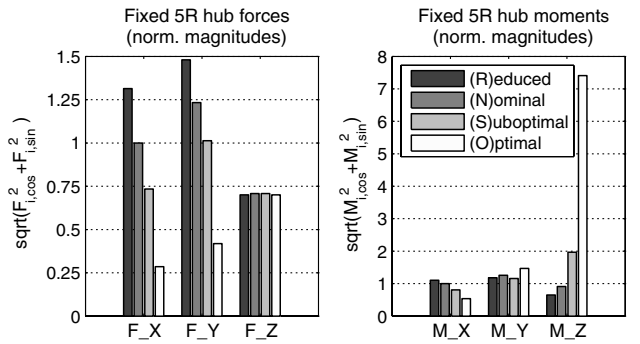

Fig. 11 Fixed $5R$ hub forces and moments for the four selected damper activity configurations.

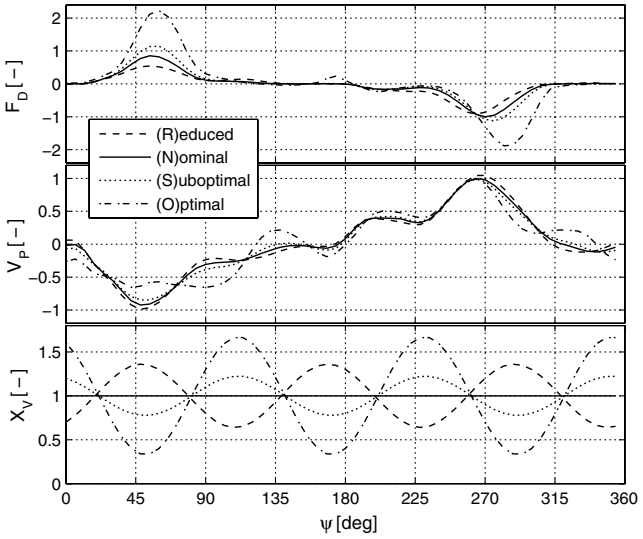

Fig. 12 Effect of the flow-restrictor activity on the damper response behavior.

values associated with the individual responses, it allows comparison of the responses within their own groups.

Figure 11 summarizes previous observations. It clearly indicates the sensitivity and tradeoff relationships mentioned in association with Figs. 8–10. The hub forces F_X and F_Y and hub moment M_Z are sensitive to the damper semi-active mode of operation, as these are the quantities affected by the changes in the in-plane rotor-blade dynamics. On the other hand, out-of-plane quantities M_X, M_Y, and F_Z are relatively insensitive to the damper semi-active operation. Figure 11 also gives a clear indication of the opposite trend between F_X and F_Y versus M_Z.

Figure 12 enables analysis of the semi-active damper in the azimuth domain. Three subplots of Fig. 12 represent the damper force F_D, the piston velocity $v_P = \mathrm{d}\dot{y}_P/\mathrm{d}t$, and the flow-restrictor opening activity x_V. These quantities are shown here for all four test cases: **O**, **S**, **N**, and **R**. Each quantity is normalized with respect to the value defined as

$$\max(\mathrm{abs}(D(\psi; \mathbf{p}_{A,N})))$$

where $D(\psi; \mathbf{p}_{A,N})$ is either F_D, v_P, or x_V computed for the test case **N** (i.e., $\mathbf{p}_A = [0, 0]$).

Two damper input quantities are v_P and x_V, where v_P is effectively external and uncontrolled excitation and represents a causal reason behind the damper force F_D. The second input to the damper is the controlled quantity x_V and it represents an internal modulated parameter of the system. Modulation of the flow-restrictor geometry allows modulation of the hydraulic resistance to the externally forced flow. However, any modulation can operate only on what is available in the form of the piston velocity v_P, including its necessary sign changes due to the reciprocal motion of the damper piston. The phase adjustment of the modulation signal therefore needs to follow the available excitation waveform v_P. This is also the case observed in Fig. 12, in which the minimum values of the opening,

$$x_{V,\min} = \min(x_{V,\mathrm{norm}}) = 1 - (\bar{p}_1^2 + \bar{p}_2^2)^{1/2}$$

are aligned with the extreme values of the external excitation, i.e., $\max(v_P)$ and $\min(v_P)$, for the cases **O** and **S**. In case **N** presented in Fig. 12, the peak piston velocities are located at $\psi_1 \approx 45°$ and $\psi_2 \approx 260°$, and the values of $x_{V,\min}$ for cases **O** and **S** are located in the similar azimuth locations. Further, $3R$ modulation frequency of the signal x_V allows the capture of both peaks observable in the piston velocity waveform v_P. The tendency to overexploit this mechanism is represented by the difference between test cases **S** and **O**, where case **O** achieves improved performance by the further reduction of $x_{V,\min}$. This mechanism, however, induces large values in the peak damper forces and is responsible for the effects observed in the previous figures. The areas with the peak values of v_P constitute the regions suitable for effective damper force modulation, and the frequency and the phase of x_V need to be matched suitably with these regions.

The case study presented in this section represents analysis of the functional behavior of the semi-active lag damper located in the rotor of the helicopter and based on the physical hydromechanical model of the damper and simple harmonic mode of the damper's semi-active operation. This study, along with [27], serves as an introductory conceptual analysis of the effects induced by the periodic modulation of the semi-active damper operating in the steady rotor environment.

VI. Conclusions

This paper discussed a damper model and its integration into an industrial rotor simulation code. Validated modeling methodology was used as a starting point for a new conceptual case study. Three specializations of generic damper model were illustrated: a reference implementation of the damper model, a refined damper model based on experiment-simulation studies, and a model of the semi-active damper with controllable flow restrictor. This paper also addressed practical implementation details for extending the simulation functionality by coupling the rotor–damper model with the helicopter rotor simulation code. The case studies documented the validity of the damper model in its passive regime and provided insights into the physical effects induced by the application of a semi-active damper with periodic perturbations. An important aspect of this paper is that all components in the simulation chain were based on physical modeling. Individually, both simulation blocks, the damper and the rotor, were validated either through their production use or through the experiment-simulation correlation. The validity of the rotor–damper coupling was documented in the parametric study of the semi-active damper with $3R$ harmonic perturbations. The physical consistency of the results (for instance, those of the optimal performance) documented the expected functional behavior of semi-active control mechanism. It was shown that external piston excitation allowed the introduction of the mechanism for a semi-active modulation of damper forces. Two main conclusions regarding the semi-active damper operation are as follows:

1) The semi-active hydraulic damper with controllable flow restrictor can significantly affect, positively or negatively, in-plane vibratory hub forces.

2) The optimal semi-active damper performance can lead to significant increases in the other rotor vibratory or instantaneous damper responses. Further, due to damper localization in the rotor system, the out-of-plane vibratory hub responses were identified as relatively insensitive to the semi-active control actions.

Previous conclusions suggest the need to specify the vibration suppression problem with a semi-active lag damper as a constrained optimization problem with parameter and response constraints. This optimization setup with coupled rotor–damper simulation code will be able to include bounds on the physically or structurally acceptable values of problem parameters as well as responses.

References

[1] Mitchell, A. H., and Johnson, K. L., "Simulation of a Hydraulic Actuator," *IBM Journal of Research and Development*, Vol. 8, No. 3, July 1964, pp. 329–334.

[2] Yao, B., Bu, F., Reedy, J., and Chiu, G. T. C., "Adaptive Robust Motion Control of Single-Rod Hydraulic Actuators: Theory and Experiments," *IEEE/ASME Transactions on Mechatronics*, Vol. 5, No. 1, March 2000, pp. 79–91. doi:10.1109/3516.828592

[3] McCloy, D., and Martin, H. R., *Control of Fluid Power, Analysis and Design*, 2nd (Revised) ed., Ellis Horwood, Chichester, England, U.K., 1980.

[4] Surace, C., Worden, K., and Tomlinson, G. R., "On the Nonlinear Characteristics of Automotive Shock Absorbers," *Proceedings of the Institution of Mechanical Engineers, Part D (Journal of Automobile Engineering)*, Vol. 206, No. 1, 1992, pp. 3–16. doi:10.1243/PIME_PROC_1992_206_156_02

[5] Audenino, A. L., and Belingardi, G., "Modelling the Dynamic Behaviour of a Motorcycle Damper," *Proceedings of the Institution of Mechanical Engineers, Part D (Journal of Automobile Engineering)*, Vol. 209, No. 4, 1995, pp. 249–262. doi:10.1243/PIME_PROC_1995_209_212_02

[6] Duym, S. W. R., "Simulation Tools, Modelling and Identification, for an Automotive Shock Absorber in the Context of Vehicle Dynamics," *Vehicle System Dynamics*, Vol. 33, No. 4, April 2000, pp. 261–285. doi:10.1076/0042-3114(200004)33:4;1-U;FT261

[7] Lee, C. T., and Moon, B. Y., "Simulation and Experimental Validation of Vehicle Dynamic Characteristics for Displacement-Sensitive Shock Absorber Using Fluid-Flow Modelling," *Mechanical Systems and Signal Processing*, Vol. 20, No. 2, February 2006, pp. 373–388. doi:10.1016/j.ymssp.2004.09.006

[8] Pekcan, G., Mander, J. B., and Chen, S. S., "Fundamental Considerations for the Design of Nonlinear Viscous Dampers," *Earthquake Engineering and Structural Dynamics*, Vol. 28, No. 11, 1999, pp. 1405–1425. doi:10.1002/(SICI)1096-9845(199911)28:11<1405::AID-EQE875>3.0.CO;2-A

[9] Yun, H.-B., Tasbighoo, F., Masri, S. F., Caffrey, J. P., Wolfe, R. W., Makris, N., and Black, C., "Comparison of Modeling Approaches for Full-Scale Nonlinear Viscous Dampers," *Journal of Vibration and Control*, Vol. 14, No. 1–2, 2008, pp. 51–76. doi:10.1177/1077546307079396

[10] Walls, J. H., "An Experimental Study of Orifice Coefficients, Internal Strut Pressures, and Loads on a Small Oleo-Pneumatic Shock Strut," NACA TN 3426, April 1955.

[11] Wahi, M. K., "Oil Compressibility and Polytropic Air Compression Analysis for Oleopneumatic Shock Struts," *Journal of Aircraft*, Vol. 13, No. 7, July 1976, pp. 527–530. doi:10.2514/3.44540

[12] Batterbee, D. C., Sims, N. D., Stanway, R., and Wolejsza, Z., "Magnetorheological Landing Gear: 1. A Design Methodology," *Smart Materials and Structures*, Vol. 16, No. 6, Dec. 2007, pp. 2429–2440. doi:10.1088/0964-1726/16/6/046

[13] Eyres, R. D., Champneys, A. R., and Lieven, N. A. J., "Modelling and Dynamic Response of a Damper with Relief Valve," *Nonlinear Dynamics*, Vol. 40, No. 2, April 2005, pp. 119–147. doi:10.1007/s11071-005-4144-6

[14] Eyres, R. D., Piiroinen, P. T., Champneys, A. R., and Lieven, N. A. J., "Grazing Bifurcations and Chaos in the Dynamics of a Hydraulic Damper with Relief Valves," *SIAM Journal on Applied Dynamical Systems*, Vol. 4, No. 4, 2005, pp. 1076–1106. doi:10.1137/040619697

[15] Eyres, R. D., "Vibration Reduction in Helicopters Using Lag Dampers," Ph.D. Dissertation, Dept. of Aerospace Engineering, Univ. of Bristol, Bristol, England, U.K., Jan. 2005.

[16] Titurus, B., and Lieven, N. A. J., "Model Validation and Experimentally Driven Hydraulic Damper Model Refinement," *Proceedings of the International Conference on Noise and Vibration Engineering*, Vols. 1–8, Katholieke Univ. Leuven, Leuven, Belgium, Sept. 2008, pp. 967–978.

[17] Bauchau, O. A., and Liu, Haiying, "On the Modeling of Hydraulic Components in Rotorcraft Systems," *Journal of the American Helicopter Society*, Vol. 51, No. 2, 2006, pp. 175–184. doi:10.4050/JAHS.51.175

[18] Grilli, R., Krishnan, R., Wereley, N. M., and Sieg, T., "Mechanisms-Based Analysis of Filled Elastomeric Dampers Under Single and Dual Frequency Excitations," *Journal of the American Helicopter Society*, Vol. 53, No. 3, 2008, pp. 252–266. doi:10.4050/JAHS.53.252

[19] Hu, W., Wereley, N. M., Chemouni, L., and Chen, P. C., "Semi-Active Linear Stroke Magnetorheological Fluid-Elastic Helicopter Lag Damper," *Journal of Guidance, Control, and Dynamics*, Vol. 30, No. 2, 2007, pp. 565–575. doi:10.2514/1.24033

[20] Hu, W., and Wereley, N. M., "Rate-Dependent Elastoslide Model for Magnetorheological Damper," *Journal of Guidance, Control, and Dynamics*, Vol. 31, No. 3, 2008, pp. 479–489. doi:10.2514/1.32732

[21] Symans, M. D., and Constantinou, M. C., "Experimental Testing and Analytical Modelling of Semi-Active Fluid Dampers for Seismic Protection," *Journal of Intelligent Material Systems and Structures*, Vol. 8, No. 8, Aug. 1997, pp. 644–657. doi:10.1177/1045389X9700800802

[22] Patten, W. N., Mo, C., Kuehn, J., and Lee, J., "A Primer on Design of Semiactive Vibration Absorbers (SAVA)," *Journal of Engineering Mechanics*, Vol. 124, No. 1, Jan. 1998, pp. 61–68. doi:10.1061/(ASCE)0733-9399(1998)124:1(61)

[23] Heo, S.-J., Park, K., and Son, S.-H., "Modelling of Continuously Variable Damper for Design of Semi-Active Suspension Systems," *International Journal of Vehicle Design*, Vol. 31, No. 1, 2003, pp. 41–57. doi:10.1504/IJVD.2003.002046

[24] Patt, D., Liu, L., Chandrasekar, J., Bernstein, D. S., and Friedmann, P. P., "Higher-Harmonic-Control Algorithm for Helicopter Vibration Reduction Revisited," *Journal of Guidance, Control, and Dynamics*, Vol. 28, No. 5, Sept.–Oct. 2005, pp. 918–930. doi:10.2514/1.9345

[25] Friedmann, P. P., and Millott, T. A., "Vibration Reduction in Rotorcraft Using Active Control: A Comparison of Various Approaches," *Journal of Guidance, Control, and Dynamics*, Vol. 18, No. 4, July–Aug. 1995, pp. 664–673. doi:10.2514/3.21445

[26] Anusonti-Inthra, P., Gandhi, F., and Miller, L., "Reduction of Helicopter Vibration Through Cyclic Control of Variable Orifice Dampers," *The Aeronautical Journal*, Vol. 107, No. 1077, Paper 2823, Nov. 2003, pp. 657–672.

[27] Titurus, B., and Lieven, N. A. J., "Modeling and Analysis of Semi-Active Dampers in Periodic Working Environments," *AIAA Journal*, Vol. 47, No. 10, Oct. 2009, pp. 2404–2416. doi:10.2514/1.41774

[28] Kamath, G. M., Wereley, N. M., and Jolly, M. R., "Characterization of Magnetorheological Helicopter Lag Dampers," *Journal of the American Helicopter Society*, Vol. 44, No. 3, 1999, pp. 234–248. doi:10.4050/JAHS.44.234

[29] Zhao, Y., Choi, Y.-T., and Wereley, N. M., "Semi-Active Damping of Ground Resonance in Helicopters Using Magnetorheological Dampers," *Journal of the American Helicopter Society*, Vol. 49, No. 4, 2004, pp. 468–482.

[30] Farhat, Ch., and Lesoinne, M., "High-Order Staggered and Subiteration Free Algorithms for Coupled Dynamic Aeroelasticity Problems," AIAA Paper 98-0515, 1998.

[31] Vaculín, O., Krüger, W. R., and Valášek, M., "Overview of Coupling of Multibody and Control Engineering Tools," *Vehicle System Dynamics*, Vol. 41, No. 5, 2004, pp. 415–429. doi:10.1080/00423110412331300363

[32] Arnold, M., "Simulation Algorithms in Vehicle System Dynamics," Martin Luther Univ. Halle, Dept. of Mathematics and Computer Science, TR 27, Halle, Germany, 2004.

[33] Hayashi, S., Hayase, T., and Kurahashi, T., "Chaos in a Hydraulic Control Valve," *Journal of Fluids and Structures*, Vol. 11, No. 6, Aug. 1997, pp. 693–716. doi:10.1006/jfls.1997.0096

[34] Young, C., "A Method of Predicting the Loading on Helicopter Rotor Blades," Royal Aircraft Establishment, TR 82096, London, Oct. 1982.

[35] Hansford, R. E., "The Development of the Coupled Rotor-Fuselage Model (CRFM)," *American Helicopter Society 48th Annual Forum*, AHS International, Alexandria, VA, June 1992, pp. 33–56.

[36] Cardona, A., and Géradin, M., "Modeling of a Hydraulic Actuator in Flexible Machine Dynamics Simulation," *Mechanism and Machine Theory*, Vol. 25, No. 2, 1990, pp. 193–207. doi:10.1016/0094-114X(90)90121-Y

[37] Géradin, M., Doan, D. B., and Klapka, I., "Mecano: A Finite Element Software for Flexible Multibody Analysis," *Vehicle System Dynamics*, Vol. 22, No. S1, 1993, pp. 87–90. doi:10.1080/00423119308969475

[38] Isakson, G., and Eisley, J. G., "Natural Frequencies in Coupled Bending and Torsion of Twisted Rotating and Nonrotating Blades," NASA CR-65, 1964.

[39] Houbolt, J. C., and Brooks, G. W., "Differential Equations of Motion for Combined Flapwise Bending, Chordwise Bending, and Torsion of Twisted Nonuniform Rotor Blades," NACA TR 1346, 1958.

[40] Hansford, R. E., "A Unified Formulation of Rotor Load Prediction Methods," *Journal of the American Helicopter Society*, Vol. 31, April 1986, pp. 58–65. doi:10.4050/JAHS.31.58